



# Triggering interfacial instabilities during forced imbibition by adjusting the aspect ratio in depth-variable microfluidic porous media

Wenhai Lei<sup>a,b</sup>, Xukang Lu<sup>a</sup>, Wenbo Gong<sup>a</sup>, and Moran Wang<sup>a,c,1</sup>

Edited by David Weitz, Harvard University, Cambridge, MA; received June 22, 2023; accepted November 5, 2023

We present a comprehensive description of the aspect ratio impact on interfacial instability in porous media where a wetting liquid displaces a nonwetting fluid. Building on microfluidic experiments, we evidence imbibition scenarios yielding interfacial instabilities and macroscopic morphologies under different depth confinements, which were controlled by aspect ratio and capillary number. We report a phenomenon whereby a smaller aspect ratio of depth-variable microfluidic porous media and lower capillary number trigger interfacial instability during forced imbibition; otherwise, a larger aspect ratio of uniform-depth microfluidic porous media and higher capillary number will suppress the interfacial instability, which seemingly ignored or contradicts conventional expectations with compact and faceted growth during imbibition. Pore-scale theoretical analytical models, numerical simulations, as well as microfluidic experiments were combined for characteristics of microscopic interfacial dynamics and macroscopic displacement results as a function of aspect ratio, depth variation, and capillary number. Our results present a complete dynamic view of the imbibition process over a full range of regimes from interfacial stabilization to destabilization. We predict the mode of imbibition in porous media based on pore-scale interfacial behavior, which fits well with microfluidic experiments. The study provides insights into the role of aspect ratio in controlling interfacial instabilities in microfluidic porous media. The finding provides design or prediction principles for engineered porous media, such as microfluidic devices, membranes, fabric, exchange columns, and even soil and rocks concerning their desired immiscible imbibition behavior.

porous media | interfacial instability | imbibition | microfluidics

Wetting fluid displacing nonwetting fluid occurs ubiquitously in natural and industrial processes at various scales, such as carbon capture (1), geological carbon sequestration (2), enhanced oil/gas recovery (3), groundwater contamination remediation (4), drug delivery in vascular networks (5), and microfluidic logic control (6). The rich variety of macroscopic displacement patterns is often the form in which interfacial instabilities are manifested, which stems from delicate interactions such as capillary, viscous, or gravitational forces at the pore scale. After a century of intense research, our understanding of driven multiphase interfaces and flow patterns remains surprisingly unbalanced. The formation of invading patterns in these typical nonlinear dissipative systems is often elucidated as a competition between the multiphase interaction energy and complex geometry (7, 8). One important displacement process is drainage, where the displaced fluid has a strong affinity to the solid. The opposite case is imbibition, where the displacing fluid has a stronger affinity to the solid surface than the displaced fluid. In contrast with the wealth of observations in incomplete drainage processes (9, 10), the emergence of incomplete invasion during imbibition was rarely observed (8, 11). Previous studies demonstrate a compact and stable pattern during imbibition (12). However, most of the imbibition mechanism research has focused on the effect of fluid properties and injection conditions (9, 13), and much less emphasis has been given to porous space, even though porous geometry has a profound influence on fluid–fluid interactions in the presence of a solid surface. In the past several tens of years, our microscopic and macroscopic description of imbibition mechanisms has been mostly limited to some seminal phase diagrams by Cieplak–Robbins or Lenormand from heuristic arguments (14–16). Recent 2-D microfluidic experiments have revisited this framework, which explored the dramatic impact of the wettability and topological features of porous structures on liquid displacement to establish an extended phase diagram (17–21). Nonetheless, we still lack a comprehensive picture of imbibition patterns and the underlying interfacial dynamics in porous media with different geometric confinements.

## Significance

Imbibition phenomena commonly take place during one wetting fluid displaces a nonwetting fluid in a porous medium—for example, a coffee bubble rises in a sugar cube, rainwater infiltrates into the soil, and carbon dioxide is stored in deep saline aquifers. However, the microscale physics and macroscopic consequences controlled by geometric confinements in heterogeneous porous media remain poorly understood. Here, we study this in detail by systematically varying depth confinements in microfluidic porous media. Our results reveal the fundamental control of interfacial instability by adjusting the aspect ratio in depth-variable microfluidic porous media. Our results open the door for unique designs in many microfluidics-related applications and elucidate the inherently pore-scale imbibition mechanism to help explain the striking macroscopic imbibition patterns.

Author contributions: M.W. designed research; W.L. and X.L. performed research; X.L., W.G., and M.W. analyzed data; and W.L. and M.W. wrote the paper.

The authors declare no competing interest.

This article is a PNAS Direct Submission.

Copyright © 2023 the Author(s). Published by PNAS. This article is distributed under [Creative Commons Attribution-NonCommercial-NoDerivatives License 4.0 \(CC BY-NC-ND\)](https://creativecommons.org/licenses/by-nc-nd/4.0/).

<sup>1</sup>To whom correspondence may be addressed. Email: [mrwang@tsinghua.edu.cn](mailto:mrwang@tsinghua.edu.cn).

This article contains supporting information online at <https://www.pnas.org/lookup/suppl/doi:10.1073/pnas.2310584120/-/DCSupplemental>.

Published December 4, 2023.

In natural and industrial processes at various scales, macroscopically porous media from 3-D to 2-D with interconnected channels or pores present a gradual enhancement of geometric constraints in one of the dimensions, as appears in the thickness direction of geological formation (22), thin rock chips (23), vascular networks (24), membranes, single-layer glass bead-packed models (25), and uniform-depth microfluidic flow cells (17). For Darcy-scale multiphase flow behavior, the capillary pressure-saturation functions as the typical imbibition response are affected by the pore size distribution, which will be limited by the macroscopic geometric confinements of porous media directly (26, 27). For pore-scale interfacial behavior, geometric confinements of porous media resulting in pore geometry variation interfere with the competition between the main meniscus and water film interface (28). It is not easy to elucidate microscale mechanisms and quantify subsurface multiphase flow dynamics in 3-D porous media because of the difficulty of direct visualization or huge computation consumption (29, 30). 2-D microfluidic experiments (11, 17) or simplified 2-D simulations (15, 16) have provided us with alternative methods for convenient and precise visualization of the fluid flow. However, theories proposed based on these 2-D experiments or 2-D simulations ignore the restrictions of porous media in the depth direction. 2-D microfluidic chip here indicates a varying size in horizontal dimensions but uniform depth in the vertical dimension, while 2-D simulations indicate there is an infinite depth in the simulation model. A few experiments and simulations have shown that depth confinement does affect the dynamics of flow instability. A simple glass isotropic etching method was proposed for square arrays connected with a shallower throat in a microfluidic chip and showed that it could promote an unstable snap-off phenomenon compared with a traditional microfluidic chip with uniform depth (31). Yet, this method is uncontrollable for the precise fabrication of complex patterns, which limits its application for a microfluidic porous media with broader and continuous pore-size distributions. Numerical simulations also reported for a modified 2-D simulation framework considering capillary and viscous force correlation in the depth direction, especially for the microfluidic flow cell, show that the geometric confinement will influence the invasion instability due to the essential capillary pressure variation in the depth direction (32).

Motivated by the importance of controlling flow patterns, and mimicking different geometric confinement in porous systems, we investigate a variant of imbibition patterns by introducing a multi-depth design in the microfluidic flow cell. In our experiments, three different microfluidic cells with the same horizontal microstructure but different depth variations are designed to control different geometric confinements in the depth direction (Fig. 1). Building on these microfluidic experiments, we first identify the emergence of incomplete imbibition patterns triggered by the small aspect ratio in strong depth-variable microfluidic porous media, and these phenomena can be suppressed by the large aspect ratio in uniform-depth microfluidic chips. Here, the aspect ratio  $R_{asp} = W/D$  was defined as the ratio of channel width  $W$  and depth  $D$ . We find that the displacement becomes incomplete at small capillary number  $Ca$  due to the instability of water film flow along the corner, also called corner flow, on the solid surfaces in porous media. Strong depth confinement has a suppressing effect on this interfacial instability: Increasing the medium's depth confinement results in lower critical  $Ca$  of dramatic transition from incomplete flow patterns to complete patterns. We further proposed a pore-scale theory to explain the impact of depth variation, aspect ratio, and capillary number on microscopic interfacial instability, which is also validated by pore-scale numerical simulations and microfluidic experiments. By

inputting pore-scale flow events in macroscopic porous media, we evidence and explain that these macroscopic patterns stem from these microscopic interfacial dynamics. Our results reveal the fundamental control of interfacial instability during forced imbibition by adjusting the aspect ratio of porous media with different geometric confinements, which involves key physical mechanisms that are essential in applications.

## Results and Discussion

**Experiments in Depth-variable Microfluidic Porous Media.** We conduct imbibition experiments in serials of microfluidic chips patterned with different depth variations (Fig. 1). The 2-D geometry of microfluidic porous media is generated randomly to reflect the statistical natural porous structure information (34). Current microfluidic devices via traditional microfabrication techniques usually contain strong constraints in the depth direction due to uniform etched depths, where the depth is chosen as the mean pore size distribution of 2-D geometry for the optative aspect ratio. To release the strong depth confinement in the microfluidic chip, we successfully developed optimized sequential photolithography to etch large pores deeper than small pores (Fig. 1A). The depth variation of the microfluidic porous structure is designed based on pore width distribution (Fig. 1B). Note that  $\alpha = d_{max}/d_{min}$  represents the depth variation factor of microfluidic porous media where  $d_{max}$  and  $d_{min}$  are the maximum and minimum depths of the microfluidic chip, respectively. A smaller depth variation factor  $\alpha$  will lead to larger aspect ratio or stronger depth confinement; therefore, there exists a hydraulic diameter limitation  $D_h = 2d_{max}$  in 3-D pore size distribution, as shown in Fig. 1C. The detailed 3-D structure of the microfluidic porous structure was characterized by the scanning electron microscope (SEM) (Fig. 1D). These 3-D microfluidic chips allow for simultaneous visualization of both the physics of wetting at the pore scale and the macroscopic imbibition pattern with a controllable and repeatable microstructure under a microscope (Fig. 1E).

Our experiment consists of injecting an aqueous liquid into a hydrophilic porous medium filled with a gaseous phase. Deionized (DI) water is used as the aqueous phase. Liquid phases are dyed for clearer visualization. Air was applied as the gaseous phase. The experimental pressure is 1 atm. The contact angle of the aqueous solution in the air can be fixed at  $\theta_0 = 10^\circ$  by thermal oxidation of the silicon surface and cleaned by piranha solution, which is the same as the bonded glass plate (SI Appendix, Fig. S4). The microscopic capillary number  $Ca_{micro} = \eta_{water} v_{inj} / \gamma$ , where  $\eta_{water} = 1.0$  mPa·s is the viscosity of water, the viscous ratio is  $M = \eta_{air} / \eta_{water} \approx 0.018$ ,  $\gamma = 71$  mN/m is the interfacial tension between water and air,  $v_{inj} = Q / (DW\phi)$  is the characteristic injection velocity for a depth  $D = 40$   $\mu$ m at the inlet porous part, the width of microfluidic chip  $W = 6$  mm, and the porosity  $\phi = 0.38$  at the inlet cross-section. Note that  $\gamma / \eta_{water}$  is a characteristic flow velocity that depends only on the fluid properties. The macroscopic capillary number  $Ca_{macro} = \eta_{water} \phi v_{inj} L / kP_c = Ca_{micro} \phi LR / 2k$  is defined by the balance of viscous force and capillary force on microfluidic porous media (35, 36), where  $P_c = 2\sigma/R$  is the characteristic capillary force,  $R = 30$   $\mu$ m is the characteristic hydraulic radius for a uniform-depth microfluidic chip,  $L = 8$  mm is the length of porous media, and  $k = 2.9 \times 10^{-12}$  m<sup>2</sup> is the permeability for the uniform-depth microfluidic chip, the macroscopic capillary numbers of different microfluidic chip structures are similar (SI Appendix, Text SI.2). By varying the injection rate ( $Q = 100, 10, 1.0, 0.10$   $\mu$ L/min), we conduct experiments at four capillary numbers spanning 3 orders of magnitude ( $Ca_{micro} = 2.6 \times 10^{-4}, 2.6 \times 10^{-5}, 2.6 \times 10^{-6}$ ,

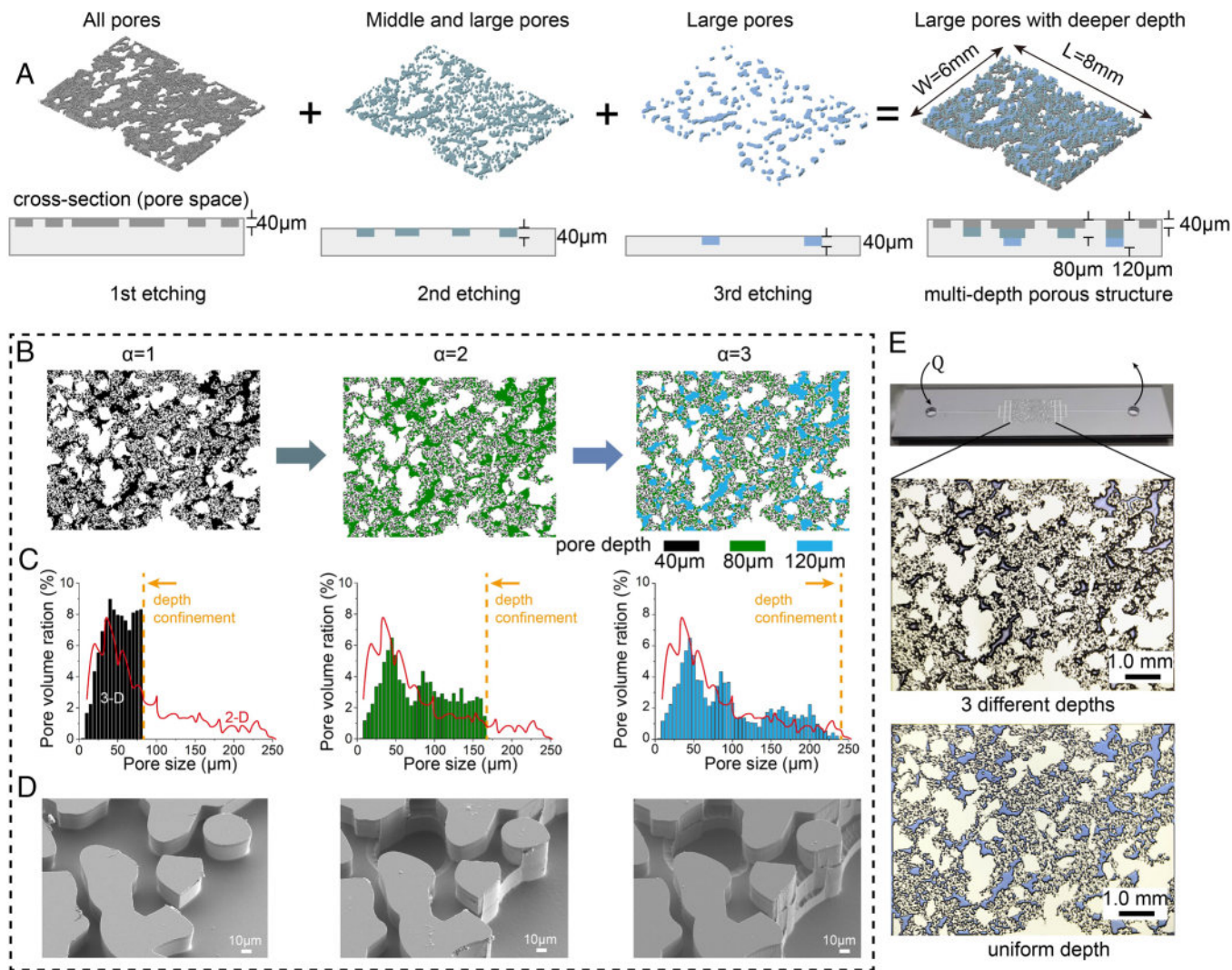


**Fig. 1.** We design microfluidic chips with different depth variations by optimized sequential photolithography. (A) Schematic showing the strategy for the fabrication of depth-variable microfluidic chip by optimized sequential photolithography and multiple etchings. (B) The porous structure will be classified into different areas based on pore width distribution, which can be etched with one, two, and three different depths. (C) 3-D pore size distributions of microfluidic chips will be compressed by different depth confinements; here, the red line is the 2-D pore-size distribution. (D) Scanning electron micrographs of the local porous structures on silicon substrates with uniform depth, two different depths, and three different depths. (E) Microfluidic chip image and corresponding porous structure observed under a microscope. The calculation of pore size distributions and pore classification for multidepth realization is obtained based on the maximal ball algorithm (33).

and  $2.6 \times 10^{-7}$ ;  $Ca_{\text{macro}} = 4.2$ ,  $4.2 \times 10^{-1}$ ,  $4.2 \times 10^{-2}$ , and  $4.2 \times 10^{-3}$ ) for each of the three different depth variation conditions ( $\alpha = 1, 2$ , and 3) described above.

#### The Transition from Incomplete to Complete Imbibition in Porous Media.

Our main result is an experimental phase diagram of the imbibition patterns obtained under different depth variation factors  $\alpha$  and a wide range of capillary numbers  $Ca$  (Fig. 2 A–L). The morphology of the imbibition patterns is a striking demonstration of depth variation controlling imbibition stability in porous media. Results show that there exists a critical line that indicates a transition in front propagation from incomplete discrete patterns to complete patterns. Incomplete discrete patterns are dominated by the corner flow, while complete patterns are controlled by the main meniscus flow. This critical line of incomplete and complete displacement can be defined by the competition between the main meniscus flow and corner flow. Here, we introduce fluid topology metrics, the Euler number, i.e.,  $\chi = \beta_0 - \beta_1 + \beta_2$  (where  $\beta_0$  is the number of objects,  $\beta_1$  is the

number of redundant loops and  $\beta_2$  is the number of cavities), as an index of the invading flow pathway morphology for the discrete flow pathway or uniform network pathway. Since the microfluidic porous media with strong depth variation ( $\alpha = 3$ ) has almost no effect on depth confinements (Fig. 1C), its complete or incomplete displacement modes can be judged by the value of  $Ca_{\text{macro}}$ . If  $Ca_{\text{macro}}$  is greater than 1, it is a complete displacement state; otherwise, it is an incomplete displacement state, which can be used to get the critical value of Euler number and water saturation. The Euler number corresponding to the transition region ( $\chi(Ca_{\text{macro}} \sim 1, \alpha = 3)$ ) is shown in Fig. 2M. Our experiments have revealed that critical  $Ca$  will increase with increasing depth variation (Fig. 2 A–L). At relatively high displacement rates with  $Ca_{\text{micro}} = 2.6 \times 10^{-4}$  or  $Ca_{\text{macro}} = 4.2$  (Fig. 2 A, E, and I), there are stable imbibition processes, resulting in almost similar complete imbibition patterns for different depth confinements, increasing  $\alpha$  can slightly enhance unstable flow, such as corner flow with low pore saturation (Fig. 2I). At ultralow capillary number  $Ca_{\text{micro}} = 2.6 \times 10^{-7}$  and  $Ca_{\text{macro}} = 4.2 \times 10^{-3}$ ,

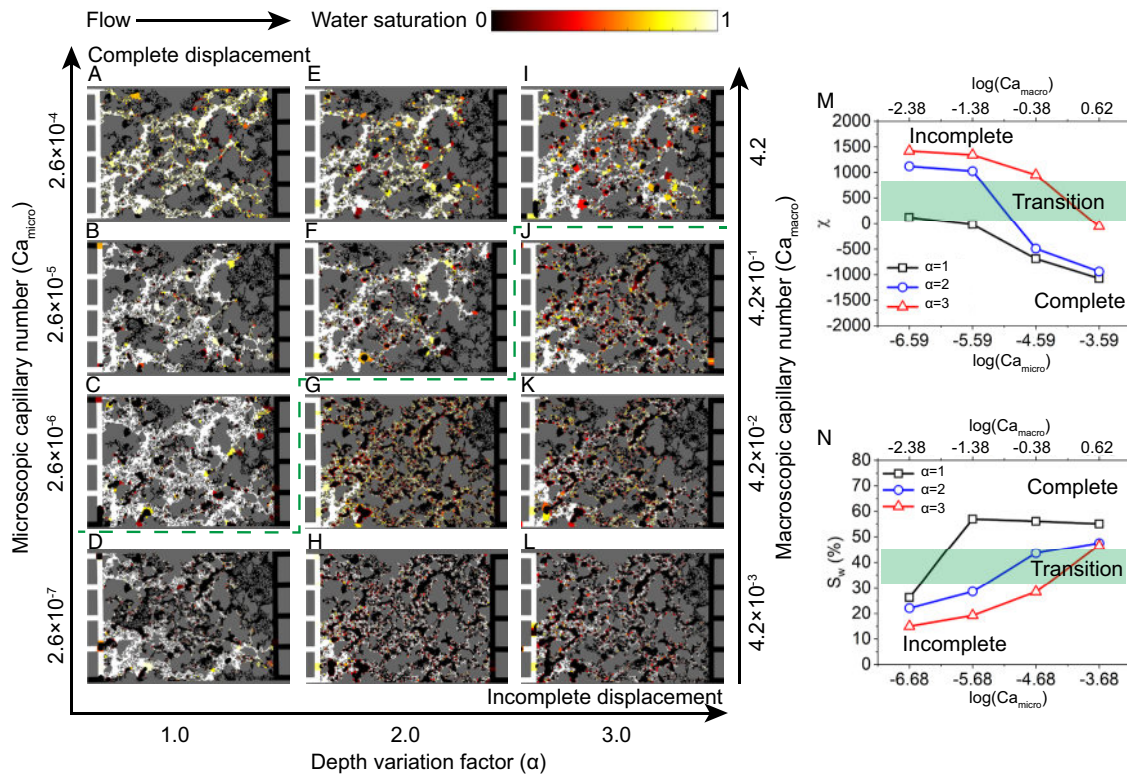


**Fig. 2.** Imbibition phase diagram in  $Ca$ - $\alpha$  space. (A–L) Imbibition patterns for microfluidic chips with different depth variation factors (left to right:  $\alpha = 1.0, 2.0, 3.0$ ) and capillary numbers (bottom to top:  $Ca_{\text{micro}} = 2.6 \times 10^{-7}, 2.6 \times 10^{-6}, 2.6 \times 10^{-5}, 2.6 \times 10^{-4}$  and  $Ca_{\text{macro}} = 4.2 \times 10^{-3}, 4.2 \times 10^{-2}, 4.2 \times 10^{-1}, 4.2$ ), where the transition part corresponds to the value of Euler number  $\chi$  where  $Ca_{\text{macro}} \rightarrow 0$  for  $\alpha = 3.0$  because of no or weak depth confinement in this case. Based on phase distribution and morphology analysis, we can get the green critical line on this phase diagram. (M) Euler number  $\chi$  and (N) wetting fluid saturation  $S_w$  of the imbibition process as a function of capillary number ( $Ca_{\text{micro}}$  and  $Ca_{\text{macro}}$ ) and  $\alpha$  at the breakthrough stage. These patterns correspond to the breakthrough stage of the experiments when the displacing fluid reaches the buffer layer of the microfluidic chip. The color map shows the pore-averaged saturation of the displacing water, where the segmentation of pores is achieved by the SNOW algorithm (37) in *SI Appendix*, Fig. S6. The corresponding phase diagram in the final stage is available in *SI Appendix*, Fig. S7. The detailed invading processes of this phase diagram have been shown in *Movie S1*.

there is no or weak stabilizing effect (Fig. 2 D, H, and L), larger  $\alpha$  present incomplete discrete patterns, and the interface between the invading water and the defending air becomes diffuse rather than sharp (Fig. 2L). However, for strong depth confinements ( $\alpha = 1$ ), they will present the hybrid state of the incomplete discrete pattern by corner flow with lower pore saturation and complete patterns by main meniscus flow under ultralow  $Ca$  (Fig. 2D). The saturation profile of the experimental phase diagram reveals that increasing  $Ca$  stable the pore-scale imbibition by higher saturation flow for all  $\alpha$  conditions (Fig. 2N). The saturation of the invading fluid increases as an increasing fraction of the defending fluid is carried out without being trapped behind. The water saturation at a complete imbibition state is significantly higher than the saturations measured at an incomplete imbibition state (Fig. 2N) and  $S_w(Ca_{\text{macro}} \sim 1, \alpha = 3)$  can also be set as the critical water saturation for complete and incomplete displacement.

Note that, in the present study, viscous instability is absent and therefore does not play a role in controlling the imbibition patterns. Our results provide insight into the control of depth confinement on imbibition stability and patterns in microfluidic porous media. Moreover, we uncover and analyze a wide range of imbibition behaviors for conditions that were rarely explored under different geometric confinements.

**Aspect Ratio Triggers Pore-scale Interfacial Instability.** Our microfluidic experimental results confirm that prescribed depth variation as well as aspect ratio can significantly affect the onset of imbibition stability. In this section, we develop microscopic snap-off criteria to describe the instability of water film during

forced imbibition processes. Such pore-scale criteria can aid in the analysis or design of structured porous media to achieve desired results depending on the applications. Mathematical models are developed for the imbibition in the ideal pore-throat channel (Fig. 3A). These models are validated by direct numerical simulations (DNSs) using computational fluid dynamics (CFD) and some microfluidic experiments, and the benchmark of simulation methods is shown in *SI Appendix*, Fig. S8.

For snap-off phenomena, the critical microscopic capillary number  $Ca_c$  is derived by the flow velocity ratio  $v^*$  of the corner flow and main meniscus flow, where the critical flow velocity ratio  $v_{\text{cir}}^* = 1$ . The flow rate of a wetting fluid along the corners of a square capillary tube can be described as (38)

$$Q_c = aC(2K)^{-\frac{1}{2}} \left( \frac{\gamma}{\eta\beta} \right)^{\frac{1}{2}} R^{\frac{5}{2}} t^{-\frac{1}{2}}, \quad [1]$$

where  $a$  is a parameter introduced by the trial function, and the parameter  $K$  is calculated by a variational method. For a rectangular tube,  $a$  and  $K$  can be chosen as 0.59 and 1.447, respectively.  $\beta$  is the dimensionless flow resistance which is a function of  $\theta$ ,  $\beta(\theta = 10^\circ) = 100.2$  (38).  $\eta$  is the viscosity of wetting fluid.

The total flow rate of a wetting fluid in the square capillary tube can be calculated as

$$Q_t = dW \frac{\gamma Ca_{\text{micro}}}{\eta}, \quad [2]$$

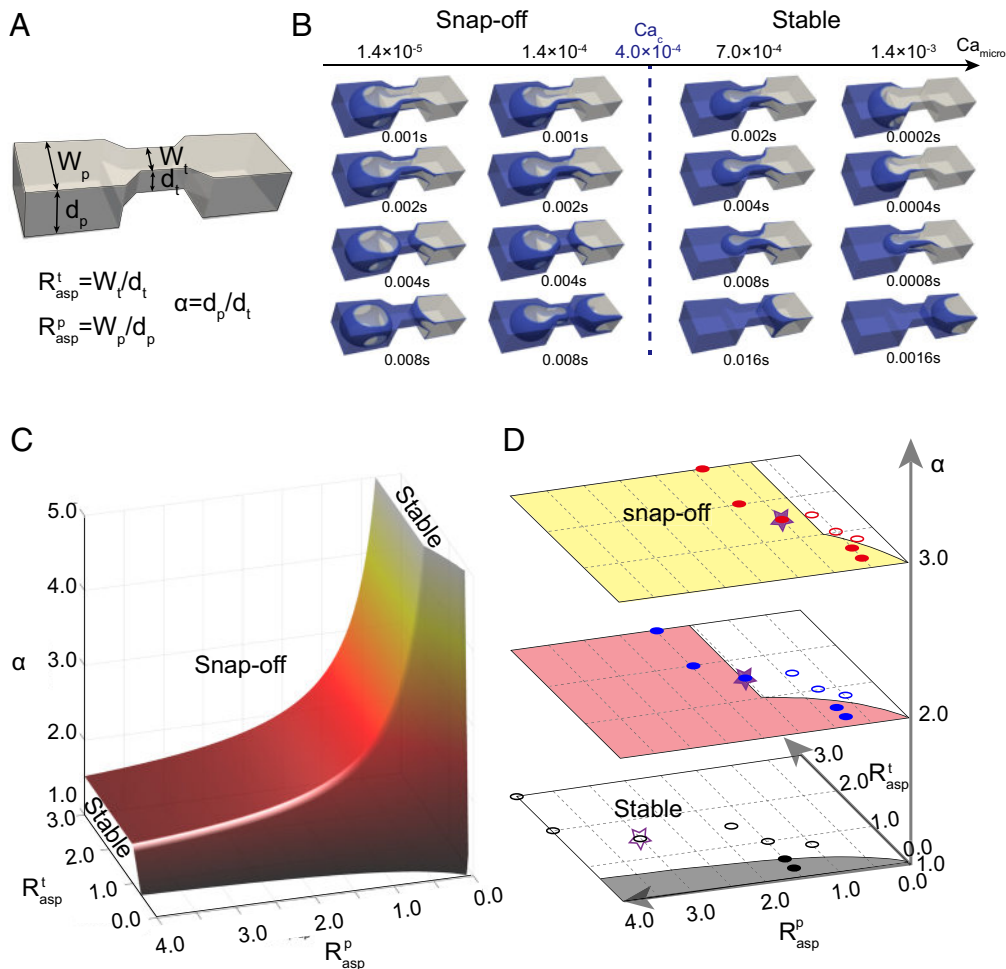


**Fig. 3.** The pore-scale phase diagram shows the stable and unstable interfacial events. (A) Schematic diagram of the pore throat structure and three dimensionless numbers,  $R_{asp}^t$ ,  $R_{asp}^p$ , and  $\alpha$ . (B) Validation of critical capillary number for the snap-off phenomena. Under strong imbibition ( $\theta = 10^\circ$ ), the capillary number will influence the relative velocity of precursor wetting films advance in the corners compared with the main meniscus. The geometry information is listed in *SI Appendix, Fig. S9*—Case 3 ( $R_{asp}^t = 1.5$ ,  $R_{asp}^p = 1$ , and  $\alpha = 3$ ). (C) The geometric criterion for snap-off phenomena in the  $R_{asp}^t$ - $R_{asp}^p$ - $\alpha$  space based on theoretical analysis; the color map represents the value of  $\alpha$ . (D) Slices of the simulation and experimental data for stable and unstable snap-off events under different geometric confinement ( $\alpha = 1, 2$ , and 3). The circle and star symbols are the results obtained by numerical simulations and microfluidic experiments respectively, where filled and open symbols represent the unstable snap-off and stable state. All the validation numerical and experimental data in the phase diagram are available in *SI Appendix, Figs. S9–S21*.

where  $d$  and  $W$  are the depth and width of the capillary tube, respectively, and the mean flow velocity can be described as  $\gamma Ca_{micro}/\eta$ . Water area of corner flow cross-section  $S = CR^2$  can be calculated by interfacial curvature radius  $R$  and the shape factor  $C = 4(\cos\theta\cos(\pi/4 + \theta)/\sin(\pi/4) - (\pi/4 - \theta))$ . The cross-section area ratio of corner flow and main meniscus flow is  $S^* = S/dW$ . When the critical flow velocity ratio of the corner flow and main meniscus flow  $v_{cir}^* = 1$ , the main meniscus flow rate  $Q_m = Q_t(1 - Q_c/Q_t) = Q_t(1 - S^*)$ .

Therefore, the ratio of the fluid volume of the corner flow  $V_c$  and main meniscus flow  $V_m$  during the imbibition time  $t$  can be calculated by

$$V^* = \frac{V_c}{V_m} = \frac{\int_0^t Q_c dt}{Q_m t} = \frac{S^*}{1 - S^*} \frac{2R^{1/2}}{(3\tau)^{1/2}} \frac{a(2K\beta)^{-1/2}}{Ca_{micro}}, \quad [3]$$

where  $\tau$  is the dimensionless time it takes for snap-off to occur, which can be calculated by  $\tau = r\gamma/3\mu R$ . Based on previous experimental investigation,  $\tau \approx 10,000$  (39).

When the critical flow velocity ratio of corner flow and main meniscus flow rate is  $v_{cir}^* = V^*/S^* = 1$ , the critical microscopic capillary number can be described as

$$Ca_c = \sqrt{2/3} a(K\beta\tau)^{-1/2} (1 - S^*)^{-1} \approx \sqrt{2/3} a(K\beta\tau)^{-1/2}. \quad [4]$$

In our framework,  $Ca_c = 4.0 \times 10^{-4}$  can be predicted and enable us to distinguish stable and unstable imbibition phenomena in the ideal pore-throat channel.

The first requirement for snap-off phenomena is  $Ca_{micro} < Ca_c$ , that is when the corner flow velocity is significantly larger than the main meniscus flow velocity, the snap-off phenomena may be triggered due to the formation of sufficient corner flow during imbibition. This first necessary condition is validated by the pore-scale simulations (Fig. 3B) and microfluidic experiments (*SI Appendix, Fig. S21*).

When Eq. 4 is satisfied that the corner flow is dominated during forced imbibition, Eq. 8 is derived to describe that the flow instability will occur at the throat part. The capillary pressure in the pore and throat can be described by the Young–Laplace equation (40). For a duct channel, we obtain the following equation (40):

$$P_{nw} - P_{wp} = 2\gamma \cos\theta \left( \frac{1}{W_p} + \frac{1}{d_p} \right), \quad [5]$$

$$P_{mw} - P_{w_t} = 2\gamma \frac{\cos\theta - \sin\theta}{\min(W_t, d_t)}, \quad [6]$$

where  $P_{w_p}$  is the water pressure in the pore channel,  $P_{w_t}$  is the threshold water pressure in the throat channel, and the air pressure  $P_{mw}$  is the same in this pore-throat channel.  $W_p$  and  $W_t$  are the width of the pore and throat channel, respectively.  $d_p$  and  $d_t$  are the depth of the pore and throat channel, respectively. When the corner flow velocity is larger than the main meniscus flow velocity (4) and the capillary force at the throat is larger than that at the pore (7), the corner flow related to air–water configuration will be unstable at the throat and any small perturbation will force the thermodynamical system to jump into merging each separate precursor interfaces; thus, the water meniscus will snap over the cross-section and divide or split the defending air phase. Eq. 8 gives the geometrical snap-off criteria for corner flow,

$$P_{w_p} - P_{w_t} = -2\gamma \left[ \cos\theta \left( \frac{1}{W_p} + \frac{1}{d_p} \right) - \frac{\cos\theta - \sin\theta}{\min(W_t, d_t)} \right] > 0, \quad [7]$$

$$\alpha > \min(R_{asp}^t, 1) \frac{(R_{asp}^p + 1)}{(1 - \tan\theta)R_{asp}^p}. \quad [8]$$

This geometry criterion for snap-off is controlled by the throat aspect ratio  $R_{asp}^t = W_t/d_t$ , the pore aspect ratio  $R_{asp}^p = W_p/d_p$ , and the depth variation factor  $\alpha = d_p/d_t$ , as shown in Fig. 3C, where  $W_p$  and  $W_t$  represent the width of the pore and throat channel, respectively.  $d_p$  and  $d_t$  represent the depth of the pore and throat channel, respectively.

We conducted various numerical simulations and microfluidic experiments for pore-throat channels with different geometries to validate these derived mathematic models. To satisfy the critical  $Ca$  requirement in Eq. 4, these simulation cases are set at  $Ca_{micro} = 10^{-5}$ . During the simulations, all channels are rectangular, and their width and depth are in the variation of pore distribution in microfluidic experiments. The depth variations and results for the snap-off in the pore-throat channel were presented and compared with the mathematical model. All data from the numerical simulations with different channel widths and depths are separated correctly by the theoretical critical surfaces (Fig. 3D). Several microfluidic experiments also valid these theoretical critical surfaces (Fig. 3D). As the depth variation ratio  $\alpha$  increases, incomplete displacement begins to be realized more easily (Fig. 3 C and D). These theoretical analyses also present some interesting and useful results that microfluidic chips with uniform depth will significantly reduce the snap-off probability. For microchips fabricated by the deep reactive ion etching (DRIE) on silicon or soft lithography on PDMS, where  $\alpha = 1$ , snap-off events are difficult to occur as shown in the gray area in Fig. 3D. Moreover, snap-off phenomena are impossible to observe on microchips fabricated by an isotropic etching method, such as HF etching on glass, where  $\alpha = 1$  and  $R_{asp}^p \& R_{asp}^t > 2$ . This also hints at why these unstable imbibition behaviors are hardly observed in traditional 2-D microfluidic chips or 2-D simulations (12, 31, 41).

**Linking Pore-scale Interfacial Instability to Macroscopic Imbibition Patterns.** The critical capillary number condition (4) and geometric condition (8) for the pore-throat channel cannot be used directly for predicting imbibition patterns in macroscopic porous media. Therefore, we reproduce the phase diagram  $Ca$ - $\alpha$

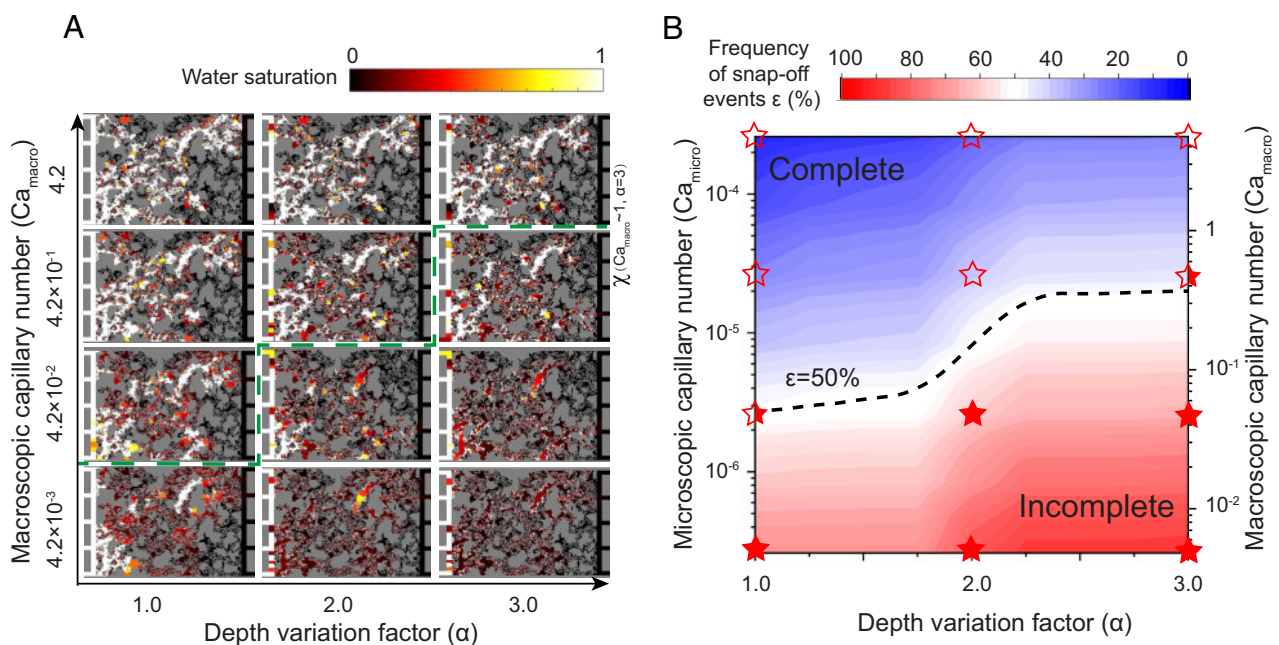


**Fig. 4.** Linking pore-scale interfacial instability to macroscopic imbibition patterns by improved dynamic pore-network model and theoretical analysis. (A) Phase diagram of the imbibition patterns was obtained by an improved dynamic pore-network model through incorporating the capillary number criteria and snap-off geometrical criteria into pore-scale flow behavior, corresponding Euler number and water saturation results are also presented in *SI Appendix, Fig. S25*. (B) Semilog plot showing the relationship between the capillary number  $Ca$  and depth variation factor  $\alpha$  by theoretical analysis. The dashed line indicates the analytically predicted critical value of the capillary number, which is a macroscopic solution based on the microscopic snap-off criterion. The snap-off frequency  $\epsilon$  equals 50% can separate the complete and incomplete imbibition patterns; the black dotted line is the contour line of  $\epsilon=50\%$ .  $\epsilon$  is calculated based on Eqs. 4 and 8 for all pore-throats in porous media, which can predict complete and incomplete regions. The star symbols are the results obtained by the microfluidic experiments, where filled ( $\epsilon \geq 55\%$ ), half-filled ( $45\% \leq \epsilon < 55\%$ ), and open symbols ( $\epsilon < 45\%$ ) represent the incomplete pattern, transition state, and complete patterns, respectively. The detailed calculation of the snap-off frequency in microfluidic experiments is shown in *SI Appendix, Fig. S26 and Tables S3 and S4*.

in microfluidic porous media by the improved dynamic pore-network model simulations, where these two conditions (Eqs. 4 and 8) are incorporated into pore-scale flow behaviors, as shown in Fig. 4A. The fundamentals of improved pore-network methods and quantification analysis of Euler number and water saturation are presented in *SI Appendix, Text SI.9 and Fig. S25*. The improved pore-network simulations clearly show the influence of pore-scale interfacial behavior on macroscopic imbibition patterns.

To quantify the influence of microscopic behaviors on macroscopic displacement patterns theoretically, we rationalize the imbibition behavior by evaluating the frequency of the snap-off events in microfluidic porous media only based on flow rate and porous geometry information in Fig. 1. We predict the transition between complete and incomplete imbibition patterns through snap-off events frequency  $\epsilon$  in the entire porous media, which was normalized by maximum snap-off events under ultralow  $Ca$  with no depth confinement (Fig. 4B). Here the snap-off frequency is calculated by the ratio of snap-off events and all throats, where pore-throats with snap-off events should satisfy both Eqs. 4 and 8. The segmentation of pores and throats is achieved by the SNOW algorithm, which can supply the pore and throat information for the geometry criteria (8). The microscopic capillary number  $Ca_{\text{micro}}$  of each pore is calculated based on the single-phase pore-network simulations for the flow rate in each pore, which will be compared with the critical microscopic capillary number  $Ca_c$  (4). The critical snap-off frequency in porous media accounting for the transition from complete to incomplete imbibition patterns is about 50%, which is also validated by the experimental results where the snap-off events are counted by water phase ganglia number (Fig. 4B and *SI Appendix, Fig. S26 and Tables S3 and S4*). Therefore, our theoretical analysis can predict the imbibition pattern only based on geometry information and injection conditions. For higher  $Ca$  and smaller  $\alpha$ , the snap-off frequency  $\epsilon$  is lower than 50%, which implies the dominance of main meniscus flow leading to complete imbibition. Conversely, for lower  $Ca$  and larger  $\alpha$ , the snap-off frequency  $\epsilon$  is higher than 50%, which implies the dominance of corner flow and frequent snap-off events leading to incomplete imbibition.

## Conclusions

We have systematically investigated the impact of geometric confinement on multiphase flow in porous media via forced imbibition experiments in patterned microfluidic porous media with multiple depths. Our results reveal the fundamental control of depth variation and aspect ratio on the nature of imbibition patterns in porous media. We show that the emergence of incomplete imbibition is controlled by  $Ca$  and  $\alpha$  under strong water-wet conditions. The imbibition pattern at low  $Ca$  is dominated by the formation of wetting films and corresponding unstable interfacial phenomena, which allows the invading fluid to propagate without filling the pore bodies. The strong depth confinement (low  $\alpha$ ) can inhibit the emergence of this unstable interfacial behavior and incomplete imbibition pattern. The critical  $Ca$  for the transition of complete and incomplete imbibition patterns increases with increasing depth variation. Our results highlight one of the inherently 3-D nature of multiphase flow in porous media, which manifests itself through physical mechanisms such as the competition between main meniscus flow and corner flow, and frequent snap-off phenomena. Our

microfluidic experiments and pore-scale numerical analyses enabled us to identify the pore-scale interfacial instability mechanisms, which can be used to explain the incomplete pattern in macroscopic porous media. However, it is worth noting that the microfluidic chip cannot be equivalent to a real 3-D porous medium principally because of its intrinsic advantage in convenient visualization (42), more 3-D structure effects, such as pores or grains connectivity, the tortuosity, and fluid flow connectivity, etc., should be introduced and analyzed in future work.

This study promotes implications for multiphase flow control in many industrial applications, from the design of microfluidic porous media to enhance fluid entrapment for biopharmacy or microchemical engineering, the design or choice of membranes to stable imbibition patterns for higher energy or mass transport efficiency, to optimizing multiphase flow in complex geologic systems. We envision potential applications related to accurate control of lubricating oil supply in spacecraft under microgravity (43), fabrication of three-dimensional periodic structures by fluid interfacial energy (44), optimization of phase distribution in geological systems (45), and more.

## Materials and Methods

**Experimental Setup.** All porous structures were fabricated from silicon material due to the small and dense geometries of the microfluidic chips in this study. The structures were created from the substrates via microfabrication techniques, including standard photolithography and inductively coupled plasma-deep reactive ion etching (ICP-DRIE). The microfluidic chips were sealed by anodically bonding thin glass to ensure visualization. To maintain the uniform wettability effect, the etched silicon wafer was then heated to 1000 °C under oxygen to create a uniform silicon dioxide layer on the etched porous structures, and both the silicon wafer and bonded glass plate were cleaned by piranha solution. The flow rate was controlled using a feedback-controlled pump (MFCS-EZ, Fluigent) equipped with a precise flow meter (Flowunit, Fluigent). The time evolution of the displacement process was recorded by a Nikon camera. Details of the microfluidic chip fabrication and characterization, flow experimental operation, and image analysis methods are described in *SI Appendix, Text SI.1-4*.

**Numerical Setup.** We study the immiscible imbibition by preformation of the Navier-Stokes equations with the open-source platform OpenFOAM, where the volume-of-fluid method (interface tracking approach) is applied and has emerged as a powerful tool for diagnosing pore-scale multiphase flow problems. In the present work, we utilized this CFD framework to investigate how the geometric confinement in the ideal pore-throat channel influences the general dynamics of two-phase flow and the stability of the imbibition front. A modified dynamic pore network was proposed by adding the critical capillary number and snap-off geometric criterion on the pore-scale events, which can reflect the macroscopic flow patterns as the microfluidic porous media. Additional details regarding the numerical algorithm employed in this study are provided in *SI Appendix, Text SI.6-9*.

**Data, Materials, and Software Availability.** All study data are included in the article and/or [supporting information](#).

**ACKNOWLEDGMENTS.** We gratefully acknowledge support from the National Key Research and Development Program of China (No. 2019YFA0708704) and a grant from the NSF of China (No. 12272207).

Author affiliations: <sup>a</sup>Department of Engineering Mechanics, Tsinghua University, Beijing 100084, China; <sup>b</sup>Department of Engineering Mechanics, KTH Royal Institute of Technology, Stockholm 100 44, Sweden; and <sup>c</sup>Department of Mechanical Engineering, Johns Hopkins University, Baltimore, MD 21218

1. M. S. Yeganeh *et al.*, Solid with infused reactive liquid (SWIRL): A novel liquid-based separation approach for effective CO<sub>2</sub> capture. *Sci. Adv.* **8**, eabm0144 (2022).
2. H. E. Huppert, J. A. Neufeld, The fluid mechanics of carbon dioxide sequestration. *Annu. Rev. Fluid Mech.* **46**, 255–272 (2014).
3. N. R. Morrow, *Interfacial Phenomena in Petroleum Recovery* (CRC Press, 1990).
4. T. Pak *et al.*, Pore-scale investigation of the use of reactive nanoparticles for in situ remediation of contaminated groundwater source. *Proc. Natl. Acad. Sci. U.S.A.* **117**, 13366 (2020).
5. A. Verma, F. Stellacci, Effect of surface properties on nanoparticle-cell interactions. *Small* **6**, 12–21 (2010).
6. O. Cybulski, P. Garstecki, B. A. Grzybowski, Oscillating droplet trains in microfluidic networks and their suppression in blood flow. *Nat. Phys.* **15**, 706–713 (2019).
7. S. E. Buckley, M. C. Leverett, Mechanism of fluid displacement in sands. *Trans. AIME* **146**, 107–116 (1942).
8. C. Odier, B. Levaché, E. Santanach-Carreras, D. Bartolo, Forced imbibition in porous media: A fourfold scenario. *Phys. Rev. Lett.* **119**, 208005 (2017).
9. J. P. Stokes *et al.*, Interfacial stability of immiscible displacement in a porous medium. *Phys. Rev. Lett.* **57**, 1718–1721 (1986).
10. D. A. Weitz, J. P. Stokes, R. C. Ball, A. P. Kushnick, Dynamic capillary pressure in porous media: Origin of the viscous-fingering length scale. *Phys. Rev. Lett.* **59**, 2967–2970 (1987).
11. B. Levaché, D. Bartolo, Revisiting the Saffman-Taylor experiment: Imbibition patterns and liquid-entrapment transitions. *Phys. Rev. Lett.* **113**, 044501 (2014).
12. K. Singh, M. Jung, M. Brinkmann, R. Seemann, Capillary-dominated fluid displacement in porous media. *Annu. Rev. Fluid Mech.* **51**, 429–449 (2019).
13. Z. Wang, J.-M. Pereira, E. Sauret, Y. Gan, Emergence of unstable invasion during imbibition in regular porous media. *J. Fluid Mech.* **941**, A40 (2022).
14. R. Lenormand, E. Touboul, C. Zarcone, Numerical models and experiments on immiscible displacements in porous media. *J. Fluid Mech.* **189**, 165–187 (1988).
15. M. Cieplak, M. O. Robbins, Dynamical transition in quasistatic fluid invasion in porous media. *Phys. Rev. Lett.* **60**, 2042–2045 (1988).
16. R. Holtzman, E. Segre, Wettability stabilizes fluid invasion into porous media via nonlocal cooperative pore filling. *Phys. Rev. Lett.* **115**, 164501 (2015).
17. B. Zhao, C. W. MacMinn, R. Juanes, Wettability control on multiphase flow in patterned microfluidics. *Proc. Natl. Acad. Sci. U.S.A.* **113**, 10251–10256 (2016).
18. B. K. Primkulov *et al.*, Signatures of fluid-fluid displacement in porous media: Wettability, patterns and pressures. *J. Fluid Mech.* **875**, R4 (2019).
19. B. K. Primkulov *et al.*, Wettability and Lenormand's diagram. *J. Fluid Mech.* **923**, A34 (2021).
20. H. S. Rabbani *et al.*, Suppressing viscous fingering in structured porous media. *Proc. Natl. Acad. Sci. U.S.A.* **115**, 4833 (2018).
21. R. Hu, T. Lan, G.-J. Wei, Y.-F. Chen, Phase diagram of quasi-static immiscible displacement in disordered porous media. *J. Fluid Mech.* **875**, 448–475 (2019).
22. S. Berg *et al.*, Real-time 3D imaging of Haines jumps in porous media flow. *Proc. Natl. Acad. Sci. U.S.A.* **110**, 3755–3759 (2013).
23. B. Ling *et al.*, Probing multiscale dissolution dynamics in natural rocks through microfluidics and compositional analysis. *Proc. Natl. Acad. Sci. U.S.A.* **119**, e2122520119 (2022).
24. Y. Fu *et al.*, Ultra-thin enzymatic liquid membrane for CO<sub>2</sub> separation and capture. *Nat. Commun.* **9**, 990 (2018).
25. K. Singh *et al.*, The role of local instabilities in fluid invasion into permeable media. *Sci. Rep.* **7**, 444 (2017).
26. M. Rücker *et al.*, Relationship between wetting and capillary pressure in a crude oil/brine/rock system: From nano-scale to core-scale. *J. Colloid Interface Sci.* **562**, 159–169 (2020).
27. T. K. Tokunaga *et al.*, Capillary pressure and saturation relations for supercritical CO<sub>2</sub> and brine in sand: High-pressure Pc(Sw) controller/meter measurements and capillary scaling predictions. *Water Resour. Res.* **49**, 4566–4579 (2013).
28. B. Zulfiqar *et al.*, The impact of wettability and surface roughness on fluid displacement and capillary trapping in 2-D and 3-D porous media: 2. Combined effect of wettability, surface roughness, and pore space structure on trapping efficiency in sand packs and micromodels. *Water Res. Res.* **56**, e2020WR027965 (2020).
29. T. Pak, I. B. Butler, S. Geiger, M. I. J. van Dijke, K. S. Sorbie, Droplet fragmentation: 3D imaging of a previously unidentified pore-scale process during multiphase flow in porous media. *Proc. Natl. Acad. Sci. U.S.A.* **112**, 1947 (2015).
30. B. Zhao *et al.*, Comprehensive comparison of pore-scale models for multiphase flow in porous media. *Proc. Natl. Acad. Sci. U.S.A.* **116**, 13799 (2019).
31. K. Xu *et al.*, A 2.5-D glass micromodel for investigation of multi-phase flow in porous media. *Lab Chip* **17**, 640–646 (2017).
32. H. Liu, S. Sun, R. Wu, B. Wei, J. Hou, Pore-scale modeling of spontaneous imbibition in porous media using the lattice Boltzmann method. *Water Res. Res.* **57**, e2020WR029219 (2021).
33. M. J. Blunt, *Multiphase Flow in Permeable Media: A Pore-Scale Perspective* (Cambridge University Press, Cambridge, 2017).
34. W. Lei *et al.*, Enhanced oil recovery mechanism and recovery performance of micro-gel particle suspensions by microfluidic experiments. *Energy Sci. Eng.* **8**, 986–998 (2020).
35. R. Hilfer, R. T. Armstrong, S. Berg, A. Georgiadis, H. Ott, Capillary saturation and desaturation. *Phys. Rev. E* **92**, 063023 (2015).
36. R. T. Armstrong, A. Georgiadis, H. Ott, D. Klemin, S. Berg, Critical capillary number: Desaturation studied with fast X-ray computed microtomography. *Geophys. Res. Lett.* **41**, 55–60 (2014).
37. J. T. Gostick, Versatile and efficient pore network extraction method using marker-based watershed segmentation. *Phys. Rev. E* **96**, 023307 (2017).
38. M. Dong, I. Chatzis, The imbibition and flow of a wetting liquid along the corners of a square capillary tube. *J. Colloid Interface Sci.* **172**, 278–288 (1995).
39. P. A. Gauglitz, C. M. St. C. J. Laurent, Radkale, An experimental investigation of gas-bubble breakup in constricted square capillaries. *J. Pet Technol.* **39**, 1137–1146 (1987).
40. R. Lenormand, C. Zarcone, A. Sarr, Mechanisms of the displacement of one fluid by another in a network of capillary ducts. *J. Fluid Mech.* **135**, 337–353 (1983).
41. L. Cha, C. Xie, Q. Feng, M. Balhoff, Geometric criteria for the snap-off of a non-wetting droplet in pore-throat channels with rectangular cross-sections. *Water Resour. Res.* **57**, e2020WR029476 (2021).
42. J. E. McClure *et al.*, Geometric state function for two-fluid flow in porous media. *Phys. Rev. Fluids* **3**, 084306 (2018).
43. E. V. Zaretsky, Liquid lubrication in space. *Tribol. Int.* **23**, 75–93 (1990).
44. H. Yasuga *et al.*, Fluid interfacial energy drives the emergence of three-dimensional periodic structures in micropillar scaffolds. *Nat. Phys.* **17**, 794–800 (2021), 10.1038/s41567-021-01204-4.
45. J. Jiménez-Martínez *et al.*, Homogenization of dissolution and enhanced precipitation induced by bubbles in multiphase flow systems. *Geophys. Res. Lett.* **47**, e2020GL087163 (2020).